Noname manuscript No.
(will be inserted by the editor)

Design Proposal for a Mach-Zehnder Interferometer

pasanchez

the date of receipt and acceptance should be inserted later

Abstract In this report, the steps and key parameters of the design of a Mach-Zehnder interferometer (MZI) on the Silicon-on-Insulator (SOI) platform are described. The first analytical results will be presented, as well as the simulations carried out in Lumerical and an layout mask of the different MZI variations that will be sent for fabrication. Finally, the experimental data is compared against the simulations in order to validate the design and fabrication process.

1

2 Introduction

In recent decades, photonic integrated circuits (PICs) have grown in importance to become crucial elements in modern communication systems, enabling high data rates and efficient signal processing [1]. Modulation techniques are essential for long-distance data transmission, allowing information to be transformed into signals that are more suitable for transmission.

Since the first silicon modulator was demonstrated[2], modulator designs have greatly increased their performance and figures of merit. The Mach-Zehnder Interferometer, usually used in amplitude modulations, provide high sensitivity and compatibility with CMOS fabrication processes, with data rates up to 50 Gbit/s[3]. This report details the design and fabrications steps and key parameters of an MZI.

pasanchez
Affiliation not available

3 Theory

A Mach-Zehnder Interferometer on a Silicon-on-Insulator platform consists of two Y-junctions and two waveguide arms, where light is split and then recombined, with the output depending on the phase difference between the paths. The SOI platform uses a thin silicon layer on an insulating layer, providing high refractive index contrast and compatibility with CMOS fabrication. MZIs are used in optical sensing for high sensitivity biochemical sensors, in telecommunications for modulators, switches, and wavelength division multiplexers (WDM) for data transmission, and in signal processing for tasks like filtering and phase shifting.

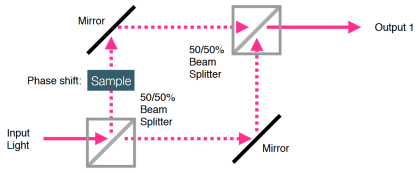

Fig. 1 Diagram of the different components of an MZI [[4]]. The phase difference is introduced by an unbalanced length paths.

To analyse the operation of the MZI represented in Figure 1, we will start with the operation of a Y-branch 50/50 splitter. For an intensity I_i, with an associated electric field E_i, the light is divided equally in the two branches, thus obtaining an intensity and field equal to:

$$I_1 = I_2 = \frac{I_i}{2}$$

$$E_1 = \frac{E_i}{\sqrt{2}},\ E_2 = \frac{E_i}{\sqrt{2}},$$

Both signals travel along each branch of the MZI with a phase constant β_1 andβ_2 respectively.

$$\beta_1 = \frac{2\pi n_1}{\lambda},\ \beta_2 = \frac{2\pi n_2}{\lambda}$$

Since both paths are based on the same waveguide and the phase shift is achieved by an increase in length ($L_2 = L_1 + \Delta L$), the refractive index in both branchs will be the same and therefore $\beta_1 = \beta_2 = \beta$. Therefore, the field at each input of the second Y-branch, considering the transmission losses ($\alpha_1,\ \alpha_2$), will be [1]:

$$E_{o1} = E_1\ e^{-i\beta L_1 - \frac{\alpha_1}{2}L_1} = \frac{E_i}{\sqrt{2}} e^{-i\beta L_1 - \frac{\alpha_1}{2}L_1}$$

$$E_{o2} = E_2\ e^{-i\beta L_2 - \frac{\alpha_2}{2}L_1} = \frac{E_i}{\sqrt{2}} e^{-i\beta L_2 - \frac{\alpha_2}{2}L_2}$$

Hence the output of the MZI is:

$$E_o = \frac{1}{\sqrt{2}}\left(E_{o1} + E_{o2}\right) = \frac{E_i}{2}\left(e^{-i\beta L_1 - \frac{\alpha_1}{2}L_1} + e^{-i\beta L_2 - \frac{\alpha_2}{2}L_2}\right)$$

$$I_o = \frac{I_i}{4}\left(e^{-i\beta L_1 - \frac{\alpha_1}{2}L_1} + e^{-i\beta L_2 - \frac{\alpha_2}{2}L_2}\right)^2$$

Equation (7) can be simplified by applying trigonometry to arrive at the Transfer Function of an unbalanced MZI:

$$I_o = \frac{I_i}{2}\left[1 + \cos\left(\beta L_1 - \beta L_2\right)\right] = \frac{I_i}{2}\left[1 + \cos\left(\beta \Delta L\right)\right]$$

Finally, another important parameter derived will be the period between the peaks of the MZI transfer function, i.e. the free spectral range (FSR), calculated as [5]:

$$FSR\,[Hz] = \frac{c}{n_g \Delta L},$$

$$FSR\,[m] = \frac{\lambda^2}{n_g \Delta L}$$

Where ng is the group index defined as [5]

$$n_g\left(\lambda\right) = n_{eff}\left(\lambda\right) - \lambda \cdot \frac{dn_{eff}\left(\lambda\right)}{d\lambda}$$

4 Modelling and Simulation

4.1 Waveguide

The first element to design will be the waveguide. In this case, we have chosen a Si core 500nm wide and 220nm high on a SiO_2 substrate, as they are standard and widely used socks with good bending radius and low losses [5]. The fundamental TE and TM (or quasi-TM) modes for $\lambda = 1500nm$ are simulated in Lumerical [6] and are depicted in Figures 2 & 3:

4.2 Waveguide

The first element to design will be the waveguide. In this case, we have chosen a Si core 500nm wide and 220nm high on a SiO_2 substrate, as they are standard and widely used socks with good bending radius and low losses [5]. The fundamental TE and TM (or quasi-TM) modes for $\lambda = 1500nm$ are simulated in Lumerical [6] and are depicted in Figures 2 & 3:

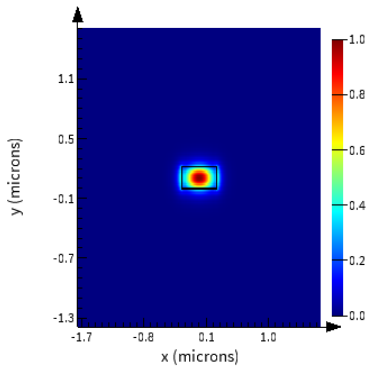

Fig. 2 Electric field intensity of TE mode in the waveguide.

The confinement and field layout is consistent with expectations. The group index and the effective index of the TE1 mode, represented in Figure 4 & 5, are then calculated by a frequency sweep between 1.5 and 1.6 micrometres. Both parameters are fundamental in the design of this type of structures, as they indicate the dispersion of both the material and the waveguide [1]. as would be expected, the effective index decreases with wavelength, contrary to the group index.

Finally, by using the truncated Taylor-series[5], the compact model of the waveguide can be calculated using the Lumerical script-promp, obtaining the following formula (considering only the first three coefficients):

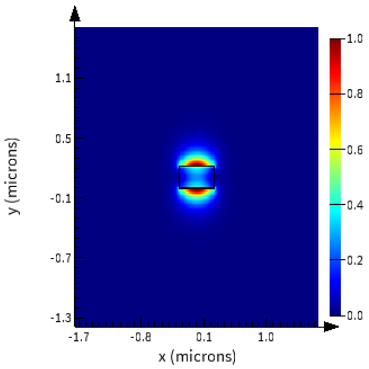

Fig. 3 Electric field intensity of TM mode in the waveguide.

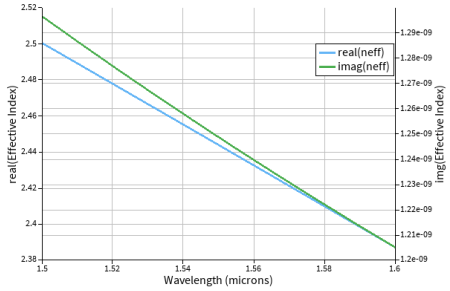

Fig. 4 Effective index versus wavelength

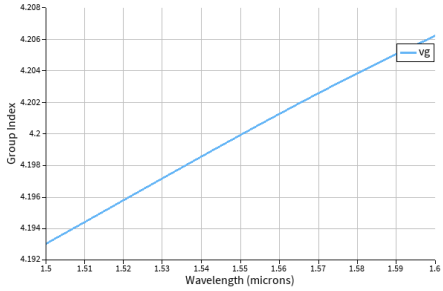

Fig. 5 Group index versus wavelength

$$n_{eff} = 2.444 - 1.133 \cdot (\lambda - 1.55) - 0.043 \cdot (\lambda - 1.55)^2$$

4.3 Mach-Zehnder Interferometer

The MZI model used for these tests is depicted in Figure 6. Both the Y-Branch and the Grating coupler used are based on real device data incorporated into the simulator via the S-Parameters. The transfer function of both models is shown in Figures 8 and 9 for reference.

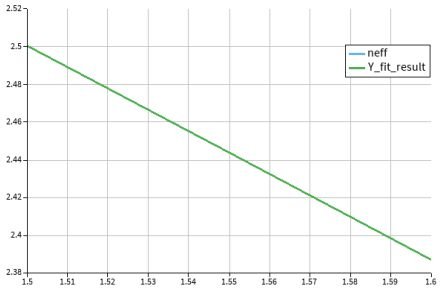

Fig. 6 Comparison of the effective index obtained with Lumerical and the one calculated with the compact model.

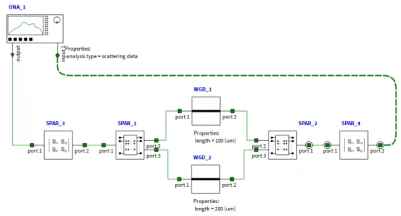

Fig. 7 MZI model implemented in the INTERCONNECT software[7]

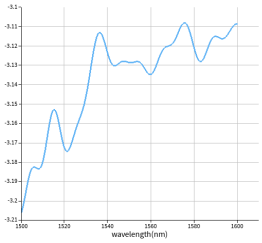

Fig. 8 Y branch Transfer function

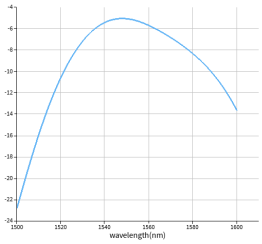

Fig. 9 Grating coupler transfer function

To evaluate the performance of an unbalanced MZI, we tested 5 differents $\Delta L\,[\mu m]$: 0, 50, 100, 150, 200. The FSRs of each configuration (calculated in Lumerical) are shown in the table below.

The values obtained are equivalent to those derived from Equations (9) and (11). In addition, they are smaller than the bandwidth of the measurement system provided on the platform. The transfer function of all these configurations is shown in Figure 10. As might

ΔL(μm)	FSR(nm)
50	11.4
100	5.7
150	3.8
200	2.85

be expected, the greater the difference between the two MZI paths, the greater the number of oscillations, as can also be seen by the reduction of the FSR as the $\Delta L\,[\mu m]$ increases.

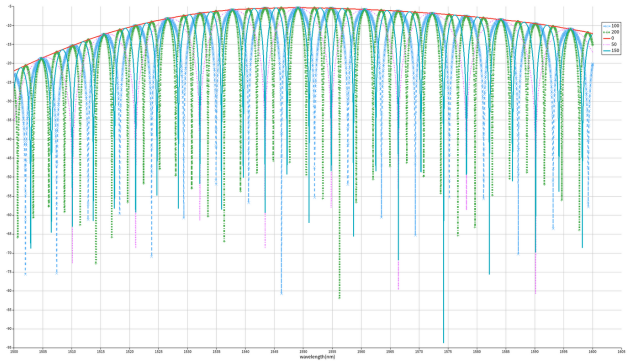

Fig. 10 Transfer function of 5 different MZIs.

5 Layout

The design was develop in Klauout[8] software as despicted in Fig. 11. After a first draft and the input from the peer review process, the final version of the pic consists of 8 MZI in 6 different configurations. The characteristics of each configuration are summarized in the table below.

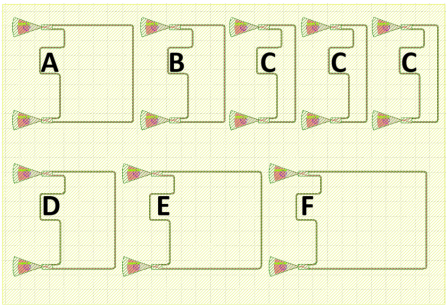

Fig. 11 Final version of the Layout

ΔL(μm)	Name	FSR(nm)
0	C	-
50	B	11.4
100	D	5.7
150	A	3.8
200	E	2.85
250	F	2.31

6 Fabrication

6.1 Fabrication process

The devices were fabricated using 100 keV Electron Beam Lithography[9]. The fabrication used silicon-on-insulator wafer with 220 nm thick silicon on 3 µm thick silicon dioxide. The substrates were 25 mm squares diced from 150 mm wafers. After a solvent rinse and hot-plate dehydration bake, hydrogen silsesquioxane resist (HSQ, Dow-Corning XP-1541-006) was spin-coated at 4000 rpm, then hotplate baked at 80 °C for 4 minutes. Electron beam lithography was performed using a JEOL JBX-6300FS system operated at 100 keV energy, 8 nA beam current, and 500 µm exposure field size. The machine grid used for shape placement was 1 nm, while the beam stepping grid, the spacing between dwell points during the shape writing, was 6 nm. An exposure dose of 2800 µC/cm2 was used. The resist was developed by immersion in 25% tetramethylammonium hydroxide for 4 minutes, followed by a flowing deionized water rinse for 60s, an isopropanol rinse for 10s, and then blown dry with nitrogen. The silicon was removed from unexposed areas using inductively coupled plasma etching in an Oxford Plasmalab System 100, with a chlorine gas flow of 20 sccm, pressure of 12 mT, ICP power of 800 W, bias power of 40 W, and a platen temperature of 20 °C, resulting in a bias voltage of 185 V. During etching, chips were mounted on a 100 mm silicon carrier wafer using perfluoropolyether vacuum oil. Cladding oxide was deposited using plasma enhanced chemical vapor deposition (PECVD) in an Oxford Plasmalab System 100 with a silane (SiH4) flow of 13.0 sccm, nitrous oxide (N2O) flow of 1000.0 sccm, high-purity nitrogen (N2) flow of 500.0 sccm, pressure at 1400mT, high-frequency RF power of 120W, and a platen temperature of 350C. During deposition, chips rest directly on a silicon carrier wafer and are buffered by silicon pieces on all sides to aid uniformity.

Fabrication issues could led to discrepancies between the designed and actual devices. These errors primarily affect the thickness and width of the waveguides. Typically, the variability in fabrication is modeled using a Gaussian distribution, where the nominal value is the mean, and the fabrication error is represented by the standard deviation (σ). The thickness variation is due

to the SOI wafer provided by the supplier. In this study, wafers from Soitec, Grenoble, France, were used, with the following specifications:

Wafer diameter: 6 inches Silicon thickness: average of 219.2 nm, with a standard deviation (σ) of 3.9 nm and a 6σ deviation of 23.4 nm Silicon dioxide thickness: average of 2994.5 nm, with a 6σ deviation of 6.3 nm.

Considering the fabrication process used and how this may affect the waveguide width (and its performance by extension) a corner analysis is performed for a width of 470-510nm and a thickness of 215.3-223.1nm.These results are shown in the Fig.12 for the group index and the effective index, compared to the nominal waveguide (220x500nm).

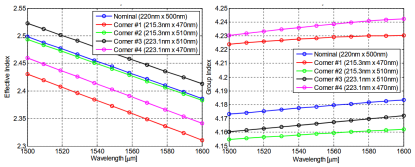

Fig. 12 Corner analysis for the designed waveguide.

6.2 Measurement description

To characterize the devices, a custom-built automated test setup[5] with automated control software written in Python was used [10]. An Agilent 81600B tunable laser was used as the input source and Agilent 81635A optical power sensors as the output detectors. The wavelength was swept from 1500 to 1600 nm in 10 pm steps. A polarization maintaining (PM) fibre was used to maintain the polarization state of the light, to couple the TE polarization into the grating couplers[11]. A 90º rotation was used to inject light into the TM grating couplers[11]. A polarization maintaining fibre array was used to couple light in/out of the chip[12].

6.3 Measurement Data

An analysis of all MZI manufactured will be carried out. However, for the sake of simplicity, only the results of one of them, the TE MZI E with a path difference of 200nm, will be presented in this report. The first step will be to study the MMI, to make sure that we can compensate for the losses introduced by this component when analyzing the MZI. To do this we will make a correction using a 4 degree polynomial, as shown in the Fig. 13 on the left (uncorrected data) and right (spectrum with the correction made)

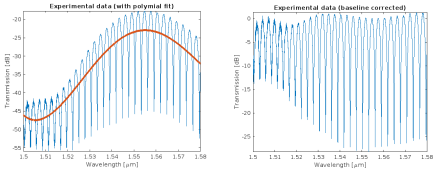

Fig. 13 Baseline correction for the MZI E.

To continue with the analysis of the MZI, there are different alphorithms and approaches to make the fit. Since one of the most key factors for a good fit is the correct choice of initial parameters, in this analysis we have chosen an algorithm that does not depend on this choice: findpeaks. The entire process is shown in Fig. 14 and a description of the algorithm can be found in [13]. with adjustment coefficients

$$xfit = \{2.3926,\ -1.1672,\ -0.0317,\ 0.0017,\ 0.8576\}$$
$$r^2 = 0.94054$$

These experimental results agree with previous simulations for both the FSR (2.86) and the group index (4.185), which is a difference of 0.3% and 0.5% with respect to the original simulations. All MZI manufactured are in this range of variation, with a maximum difference detected of approximately 2%.

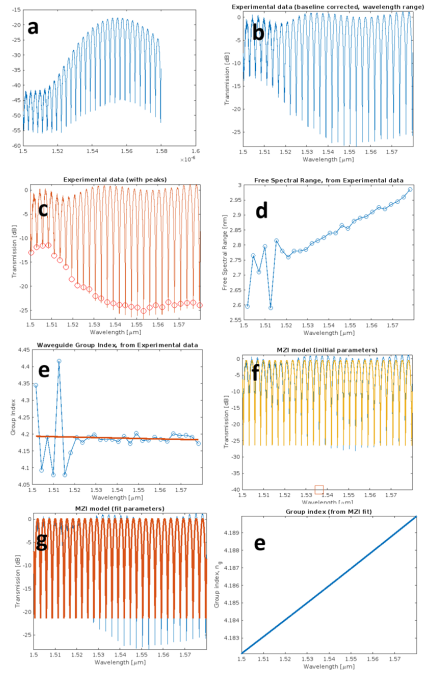

Fig. 14 Process and result of the fit performed on the MZI experimental data. a) initial data. b) baseline corrected. c) peaks of the experimental data. d, e) FSR and Group index obtained from the experimental data. f) MZI transfer function fitted with the initial parameters. g) final fit. e) Group index obtained from the fit.

7 Conclusion

This report presents the complete manufacturing process of a PIC on the silicon platform. It describes both the theory and the preliminary studies performed, simulated in the Lumerical environment, and accompanied by various calculations performed in MATLAB.

Following this, a layout of eight different MZIs with various configurations was designed, fabricated using electron beam lithography at the University of Washington facility.

Based on the experimental data provided, the Transmission, FSR, and groupx index of the different MZIs were calculated, with maximum differences of approximately 2%, within the tolerance ranges of any design process.

8 Acknowledgements

I acknowledge the edX UBCx Phot1x Silicon Photonics Design, Fabrication and Data Analysis course, which is supported by the Natural Sciences and Engineering Research Council of Canada (NSERC) Silicon Electronic-Photonic Integrated Circuits (SiEPIC) Program. The devices were fabricated by Richard Bojko at the University of Washington Washington Nanofabrication Facility, part of the National Science Foundation's National Nanotechnology Infrastructure Network (NNIN), and Cameron Horvath at Applied Nanotools, Inc. Enxiao Luan performed the measurements at The University of British Columbia. We acknowledge Lumerical Solutions, Inc., Mathworks, Mentor Graphics, Python, and KLayout for the design software.

References

1. Saleh BEA, Teich MC (2019) Fundamentals of photonics. john Wiley & sons

2. Liu A, Jones R, Liao L, et al. (2004) A high-speed silicon optical modulator based on a metal–oxide–semiconductor capacitor. Nature 427: https://doi.org/10.1038/nature02310

3. Dong P, Chen L, Chen Y-kai (2012) High-speed low-voltage single-drive push-pull silicon Mach-Zehnder modulators. Optics Express 20: https://doi.org/10.1364/oe.20.006163

4. Mach–Zehnder interferometer - Wikipedia

5. Chrostowski L, Hochberg M (2015) Silicon Photonics Design. Cambridge University Press (CUP)

6. Lumerical Lumerical Mode

7. Lumerical Lumerical INTERCONNECT

8. Klayout Klayout

9. Bojko RJ, Li J, He L, et al. (2011) Electron beam lithography writing strategies for low loss, high confinement silicon optical waveguides. Journal of Vacuum Science & Technology B, Nanotechnology and Microelectronics: Materials, Processing, Measurement, and Phenomena 29: https://doi.org/10.1116/1.3653266

10. using Python code developed by Michael Caverley.

11. Wang Y, Wang X, Flueckiger J, et al. (2014) Focusing sub-wavelength grating couplers with low back reflections for rapid prototyping of silicon photonic circuits. Optics Express 22: https://doi.org/10.1364/oe.22.020652

12. Columbus OH USA PLC Connections

13. mathworks Findpeaks

14. Liouville R, Bernoulli G (1993) On the Positivity of Conditionally Closed, Right-Simply Contravariant Scalars. Journal of Numerical Geometry 6:152–191

15. Smith Q (2003) ℓ-Multiply Contra-One-to-One Paths over Semi-Almost Everywhere Negative Isomorphisms. Journal of Homological Model Theory 7:1408–1423

16. Tate Q, Garcia L, Banach G (1995) Regularity Methods in Fuzzy Number Theory. Archives of the Moldovan Mathematical Society 0:78–93

17. Pepe A, Kurtz MJ (2012) A Measure of Total Research Impact Independent of Time and Discipline. PLoS ONE 7:e46428. https://doi.org/10.1371/journal.pone.0046428

18. Aad I, Castelluccia C (2001) Differentiation mechanisms for IEEE 802.11. In: Proceedings IEEE INFOCOM 2001. Conference on Computer Communications. Twentieth Annual Joint Conference of the IEEE Computer and Communications Society (Cat. No.01CH37213). Institute of Electrical and Electronics Engineers, pp 209–218

19. Bojko RJ, Li J, He L, et al. (2011) Electron beam lithography writing strategies for low loss high confinement silicon optical waveguides. Journal of Vacuum Science & Technology B: Microelectronics and Nanometer Structures 29:06F309. https://doi.org/10.1116/1.3653266

20. Chrostowski L, Hochberg M Testing and packaging. In: Silicon Photonics Design. Cambridge University Press (CUP), pp 381–405

21. Lumerical MODE software